

Waveguide-integrated black phosphorus photodetector with high responsivity and low dark current

Nathan Youngblood, Che Chen, Steven J. Koester and Mo Li*

Layered two-dimensional materials have demonstrated novel optoelectronic properties and are well suited for integration in planar photonic circuits. Graphene, for example, has been utilized for wideband photodetection. However, because graphene lacks a bandgap, graphene photodetectors suffer from very high dark current. In contrast, layered black phosphorous, the latest addition to the family of two-dimensional materials, is ideal for photodetector applications due to its narrow but finite bandgap. Here, we demonstrate a gated multilayer black phosphorus photodetector integrated on a silicon photonic waveguide operating in the near-infrared telecom band. In a significant advantage over graphene devices, black phosphorus photodetectors can operate under bias with very low dark current and attain an intrinsic responsivity up to 135 mA W⁻¹ and 657 mA W⁻¹ in 11.5-nm- and 100-nm-thick devices, respectively, at room temperature. The photocurrent is dominated by the photovoltaic effect with a high response bandwidth exceeding 3 GHz.

wo-dimensional materials have tremendous potential for optoelectronic applications¹. Graphene, the most extensively investigated two-dimensional material, has many novel optical properties, including a tunable interband transition and saturable absorption, and has potential for a wide range of optoelectronic applications^{2,3}. However, one important optoelectronic device application where graphene is severely limited is in photodetection. Although graphene has demonstrated broadband optical absorption, an ultrafast photoresponse and reasonable responsivity4-7, graphene photodetectors have a very high dark current when they are operated in the photoconductive mode where a bias voltage is applied to attain high responsivity^{7,8}. This is a direct result of the lack of a bandgap in graphene. This high dark current leads to high shot noise, the dominant noise source at low levels of light, and thus sets the noise floor of the photodetector at a high level. Other two-dimensional materials such as layered transition-metal dichalcogenides (TMDCs) have relatively large bandgaps, so they do not absorb at the important telecom wavelengths^{9–12}.

Black phosphorus (BP) is a layered crystal of phosphorus that is stable at room temperature. It has recently been the subject of interest after experiments showed that few-layer and monolayer flakes can be exfoliated in a similar manner to graphene 13-15. In contrast to graphene, however, BP has a direct bandgap that is predicted to be 1.8-2.0 eV for the monolayer. As the number of layers increases, the bandgap reduces and eventually reaches ~0.3 eV in bulk^{16,17}. Such a layer-tunable bandgap covering the visible to mid-infrared spectral range suggests that BP is a very promising two-dimensional material for broadband optoelectronic applications^{18–21}. BP has also shown excellent electrical properties, including a high hole mobility up to 1,000 cm² V⁻¹ s⁻¹ at room temperature, an on-off ratio up to 105, and good current saturation in field-effect devices 13-15,22. In this Article we integrate a few-layer BP photodetector into a silicon photonic circuit, which also enables quantitative measurement of the absorption and quantum efficiency of BP in the telecom band (~1.55 μm). Operated in the photoconductive mode, high responsivity, high internal quantum efficiency and operation at bit rates above 3 Gbit s⁻¹ are achieved with very low dark currents.

To most efficiently utilize the optoelectronic properties of two-dimensional materials it is necessary to integrate them on planar photonic devices so that the optical interaction length is not bound by the thickness of the materials^{6,7,23–26}. Here we integrate a BP field-effect transistor (FET) on a silicon photonic waveguide using few-layer graphene as the top-gate. In this way, the carrier type and concentration in the BP layer can be electrostatically tuned, allowing the mechanism of photocurrent generation to be investigated and the performance of the device to be optimized. Figure 1a presents the structure of the device, showing the BP channel and graphene top-gate, and Fig. 1b shows an optical image of the complete device. The silicon photonic circuit patterned on the silicon-on-insulator (SOI) substrate includes a Mach-Zehnder interferometer (MZI), which allows the absorption in the BP to be quantitatively measured in order to unequivocally determine the intrinsic responsivity and internal quantum efficiency^{23,24}, which are more useful than the extrinsic values in revealing BP's true potential for optoelectronic applications. After planarization of the substrate with SiO₂, the BP layer was exfoliated from bulk crystal and transferred onto one of the optical arms (one measurement arm, one reference arm) of the MZI using a wet transfer method²⁷. Figure 1c presents an atomic force microscope image of the BP layer transferred onto the waveguide after deposition of source and drain contacts made of Ti (5 nm) and Au (50 nm). The width of the BP is $6.5\,\mu m$ and the thickness was determined to be $11.5\,n m$ from the profile in Fig. 1c, indicating it is composed of about 23 layers. During each step of fabrication (Fig. 1d) the transmission spectrum of the MZI was measured. From the extinction ratio (ER) measured from the interference fringes in the spectra, the absorption loss in the measurement arm of the MZI can be determined using the relation ER = $(1 + e^{\alpha \Delta L/2})^2/(1 - e^{\alpha \Delta L/2})^2$, where α is the absorption coefficient and ΔL is the width of the BP FET. The results are shown in Fig. 1d. From measurements taken after transfer of the BP and deposition of the top-gate dielectric (see Methods), we determined that the absorption coefficient in the BP in the device is 0.182 dB µm⁻¹. This result confirms that few-layer BP has strong absorption in the near-infrared, as expected from its narrow

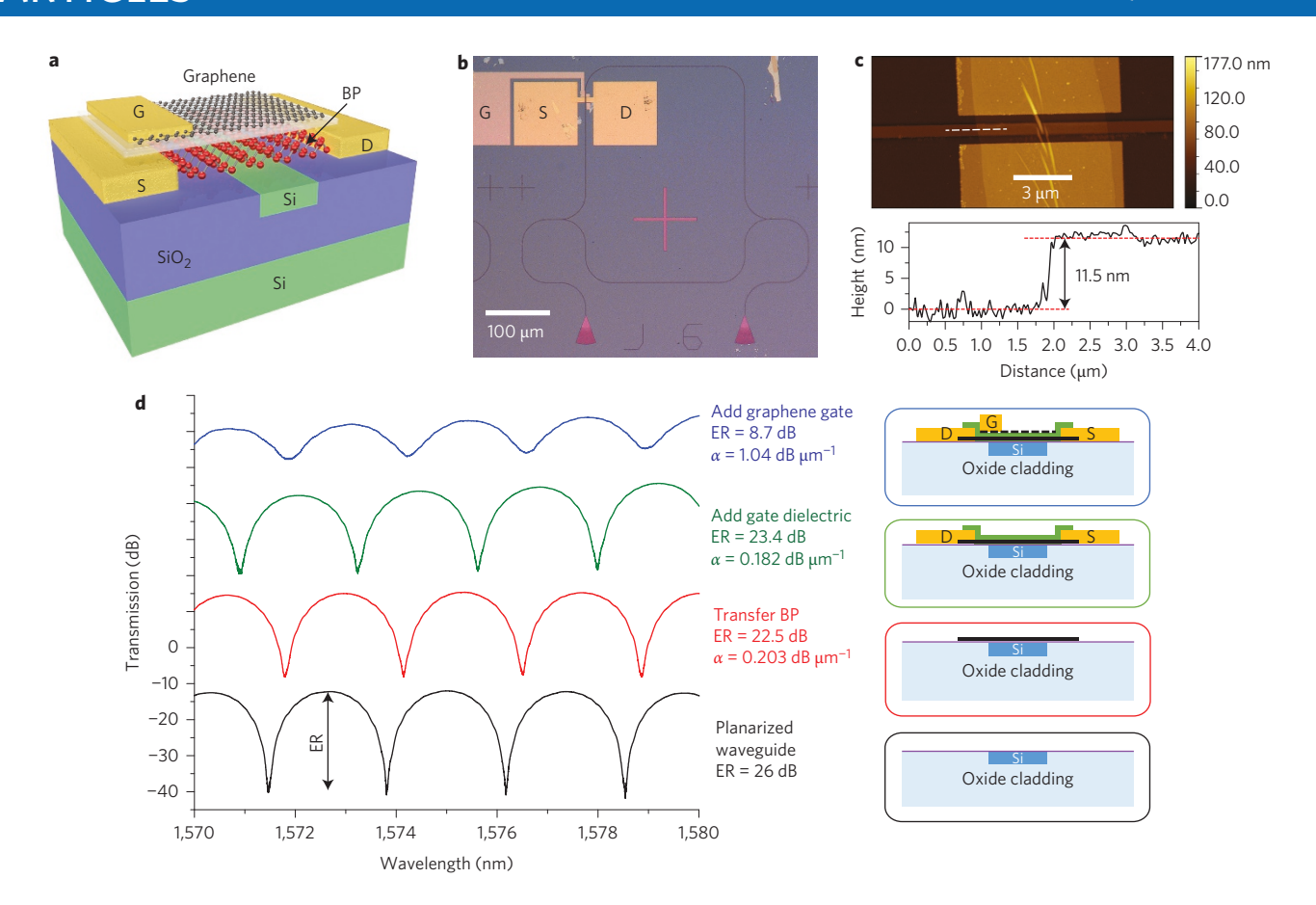


Figure 1 | BP photodetector integrated in a silicon photonic circuit. a, Three-dimensional illustration of the device configuration, featuring a few-layer graphene top-gate. **b**, Optical microscope image of a complete device. A BP field-effect transistor is integrated in one arm of an MZI circuit. **G**, gate; S, source; D, drain. **c**, Top: atomic force microscope image of the BP with contacts and before the deposition of gate dielectrics and fabrication of the top-gate. Bottom: height profile along the white dashed line in the top panel, showing that the thickness of the BP is 11.5 nm, corresponding to 23 monolayers. **d**, Transmission spectra of the MZI measured after each step of fabrication (shown in the schematics to the right). Spectra have been vertically translated for clarity. From the extinction ratio, the absorption coefficient of each added layer can be determined. Using this method, the absorption coefficient of the BP in the completed device is determined to be 0.182 dB μm⁻¹.

bandgap¹⁹. The 6.5- μ m-long device absorbs 78.7% of the optical power in the waveguide, of which 17.5% is absorbed by the BP and the rest by the graphene top-gate, which is the main cause of loss. However, such a top-gate is unnecessary in practical devices if the initial doping in the BP can be optimized, for example, by chemical doping.

We first performed field-effect transport measurements of the device to characterize its electrical properties. The source-drain current I_{DS} , measured while sweeping the gate voltage V_G at various fixed bias voltages $V_{\rm DS}$, is shown in Fig. 2a. The ambipolar transport behaviour of the BP is clearly shown. The minimum conductance point at $V_G = -7$ V reveals that the BP is n-doped with an electron concentration estimated to be $1.6 \times 10^{13} \, \text{cm}^{-2}$. We have consistently found that in devices using top-gates with an Al₂O₃ gate dielectric grown by atomic layer deposition (ALD), the BP is n-doped (Supplementary Section 4). This contrasts with the p-doped BP observed in most back-gated devices reported in the literature to date^{13–15}, and in devices that we have made using HfO₂ as the top-gate dielectric. We therefore speculate that the doping type and level in BP are sensitive to the types of dielectric layers above and below the BP as well as the deposition conditions of those layers. This relationship will require more systematic studies to draw meaningful conclusions but is not the focus of this work. With the configuration of a top-gate and thin gate dielectric, the source-drain current of our device can be efficiently modulated by the gate voltage with an on-off ratio of 500 similar to other

devices with comparable BP thicknesses^{14–16}. However, unlike BP devices using a bottom-gate^{13–15}, the field-effect characteristics (Fig. 2a) of our top-gated BP FET show much higher conductance on the electron side when a large positive gate voltage is applied than on the hole side. Also, the source–drain I–V relation is linear when the BP is n-doped but nonlinear when the BP is p-doped (Fig. 2b,c). This indicates that the Schottky barrier at the contact–BP interface is lower when the BP is n-doped than when the BP is p-doped. This can be attributed to the effects induced by capping the BP with the Al_2O_3 gate dielectric layer²⁸. Additionally, the fact that the I–V characteristics are mostly symmetric about the positive and negative source–drain voltage reflects that the two contacts are nearly identical. Therefore, excellent transport properties and efficient tuning of the carrier type and concentration in BP are achieved in our device.

We next measured the BP device's response to optical signals in the waveguide. A tunable diode laser was fibre-coupled to the grating couplers, which have a coupling efficiency of ~25%. Figure 3a shows the I-V characteristics of the device at various optical power levels and with $V_{\rm G}=-8$ V so the BP is nearly intrinsic. It can be clearly seen that significant photocurrent, positive relative to $V_{\rm DS}$, is generated when the optical signal is on. The positive sign of the photocurrent suggests that the generation mechanism is photovoltaic8.29,30. The photo-thermoelectric effect can be ruled out as the photogeneration mechanism because the device is symmetric between the source and drain contacts8.21,31.

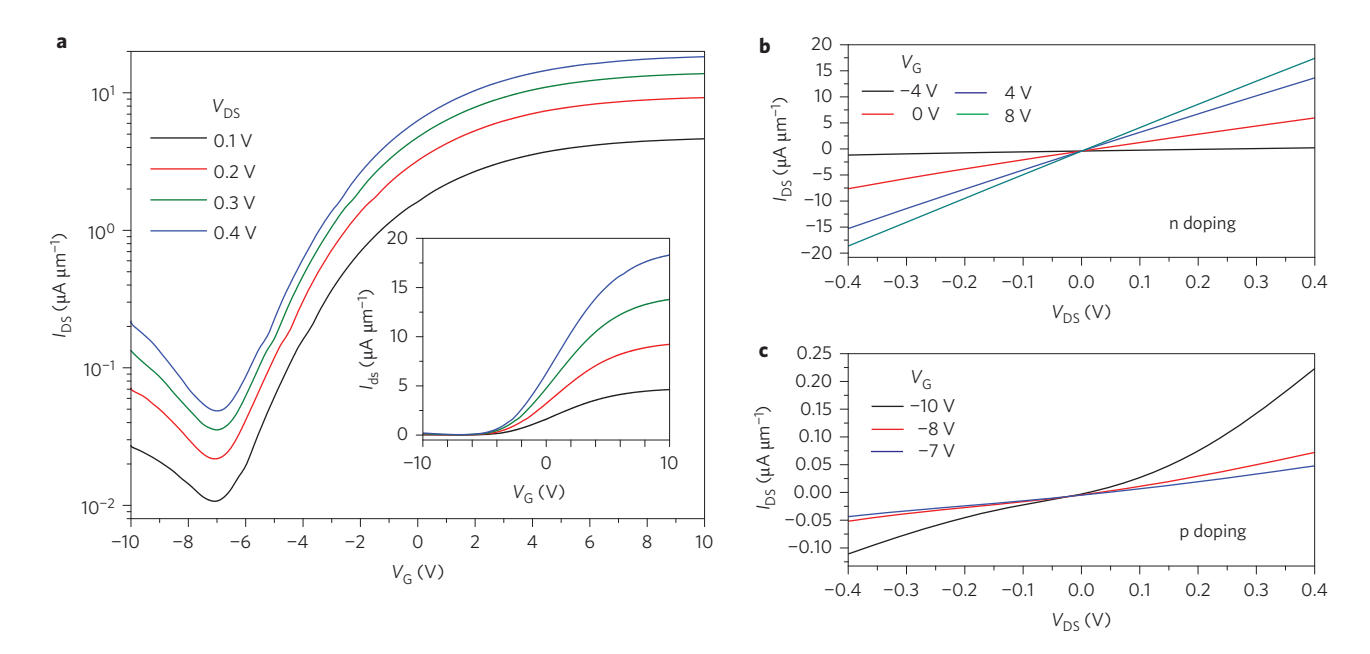


Figure 2 | **Field-effect characteristics of the BP photodetector. a**, Source-drain current, I_{DS} , of the device at various fixed bias voltages, V_{DS} , as the gate voltage, V_G , is swept. Inset: linear-scale plot of the main panel. **b,c**, I-V characteristics of the device when the BP is gated to be n-doped (**b**) and p-doped (**c**), respectively.

However, when V_G is increased to be more positive so the BP is gated to be more heavily n-doped, as shown in Fig. 3b, the sign of the photocurrent changes to negative relative to $V_{\rm DS}$. The sign change suggests that the photocurrent generation mechanism is no longer photovoltaic, but is due to the bolometric effect, which stems from the decrease in conductance when the BP is heated by optical absorption. This bolometric effect is similar to that observed in biased graphene photodetectors, in which the reduction of conductance at elevated temperatures is attributed to increased phonon scattering^{8,21}. Compared with graphene, it appears that the bolometric photocurrent in BP at high doping is much weaker than the photovoltaic current at low doping. This is attributed to the higher quantum efficiency in BP than that found in graphene. (For a detailed comparison with other published works on the origin of the photoresponse in BP, see Supplementary Section 7.)

To further illustrate these two distinct regimes of photogeneration, we systematically measured the photocurrent at various gate and bias voltages with a fixed optical power of 1.91 mW. The results are plotted in Fig. 3c. The change of photocurrent sign with gate voltage is clearly seen for all bias voltages. At low doping ($-10 \text{ V} < V_G < -1 \text{ V}$), the photocurrent is strong and dominated by the photovoltaic current, whereas at high n-type doping $(V_{\rm G} > 0 \text{ V})$, the photocurrent is weak, opposite the bias voltage and dominated by the bolometric effect. We calculated the intrinsic responsivity and internal quantum efficiency using the actual amount of optical power absorbed by the BP (determined from interferometry results). As can be seen from Fig. 3d, optimal performance is achieved when the BP is gated to be nearly intrinsic (when $V_G = -8 \text{ V}$) and under a large bias voltage ($V_{\text{bias}} = V_{\text{DS}} =$ -0.4 V), where it achieves the best intrinsic responsivity of 135 mA W⁻¹ and internal quantum efficiency of 10%. However, taking the absorption by the graphene top-gate into account, the overall extrinsic responsivity of the device is reduced to 18.8 mA W⁻¹. Higher responsivity could be achieved with a larger bias voltage, but, because the applied gate voltage is high, the bias voltage was not increased beyond ±0.4 V to avoid the risk of breaking down the gate dielectric. In another device with 100-nm-thick BP and no top-gate (Fig. 3e), an intrinsic responsivity up to 657 mA W⁻¹

and internal quantum efficiency up to 50% are achieved at +2 V bias voltage (Supplementary Section 5).

Importantly, due to the finite bandgap in BP, the dark current of our device is very low. At the optimal operation condition $(V_{\rm G} = -8 \text{ V}, V_{\rm bias} = -0.4 \text{ V})$ the dark current $(I_{\rm dark})$ is only 220 nA, which is more than three orders of magnitude less than that of a graphene photodetector under similar bias voltage^{5,8}. Taking the external responsivity into account, the normalized photocurrentto-dark-current ratio (NPDR)³² of our BP photodetector is plotted in the inset of Fig. 3a. At $V_{\rm bias}$ = -0.4 V, the NPDR of our BP photodetector is 85 $\mbox{mW}^{-1},$ which is four orders of magnitude higher than that of typical graphene devices^{5,7}. This value of NPDR is also comparable to that of waveguide-integrated Ge photodetectors of a similar configuration³³ and could be improved by an order of magnitude if the top-gate absorption loss were eliminated. Although graphene photodetectors can be operated in the photovoltaic mode at zero bias, with zero dark current but with a substantially compromised responsivity^{5,7}, the low resistance of graphene leads to high Johnson current noise from the shunt resistance. In comparison, the source-drain shunt resistance of our BP photodetector is very high $(R_{SD} > 1 \text{ M}\Omega)$, so the noise of the photodetector is dominated by dark-current shot noise. Thus, in terms of both responsivity and noise level, the BP photodetector has significant advantages over its graphene counterparts.

The frequency response of the photocurrent can also help reveal the mechanism of photocurrent generation. Figure 4a shows the normalized response of the photodetector to an amplitude-modulated optical signal over a broad frequency range from 10 Hz to 10 GHz, measured using a lock-in amplifier (for less than 100 kHz) and network analysers (for 100 kHz to 10 GHz) while fixing the bias voltage ($V_{\rm bias} = 0.4 \, \rm V$). When the BP is gated with $V_{\rm G} = -8 \, \rm V$ to be nearly intrinsic, the photodetector shows a high-speed response with a roll-off frequency measured to be $f_{\rm -3dB} = 2.8 \, \rm GHz$, which is limited by the RC bandwidth of the device as well as the bandwidth of the measurement instruments (including the current amplifier and bias tee). This fast response is expected for the photovoltaic mechanism of photocurrent generation, which is fundamentally limited by the carrier recombination time in BP and is accelerated by the bias field. In stark contrast, when

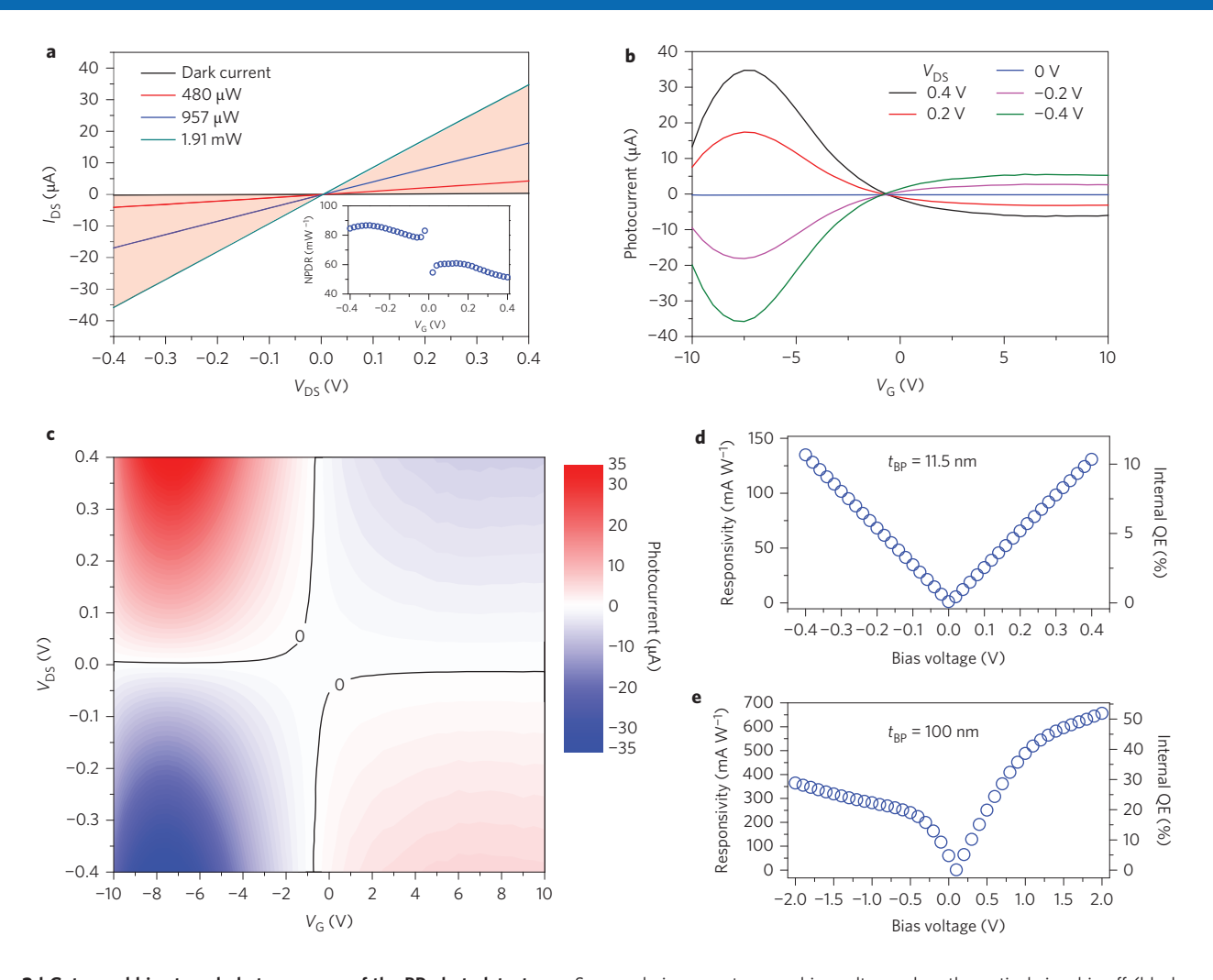


Figure 3 | Gate- and bias-tuned photoresponse of the BP photodetector. a, Source-drain current versus bias voltage when the optical signal is off (black line) and at various power levels (red, $480 \mu W$; blue, $957 \mu W$; green, 1.91 m W). Gate voltage, -8 V. Inset: normalized photocurrent-to-dark-current ratio (NPDR) for an optical power of 1.91 m W. b, Photocurrent versus gate voltage at fixed bias voltages (1.91 m W) optical power). The sign of the photocurrent changes as the gate voltage increases from negative values (where the BP has low doping) to positive (where the BP is highly n-doped). c, Two-dimensional contour plot of the photocurrent as a function of gate and bias voltages. Photocurrent generation is dominated by the photovoltaic and bolometric effects in regions with low and high doping, respectively. d, Intrinsic responsivity and internal quantum efficiency (QE) versus applied bias for 11.5-nm- and 100-nm-thick BP. t_{BP}, thickness of BP.

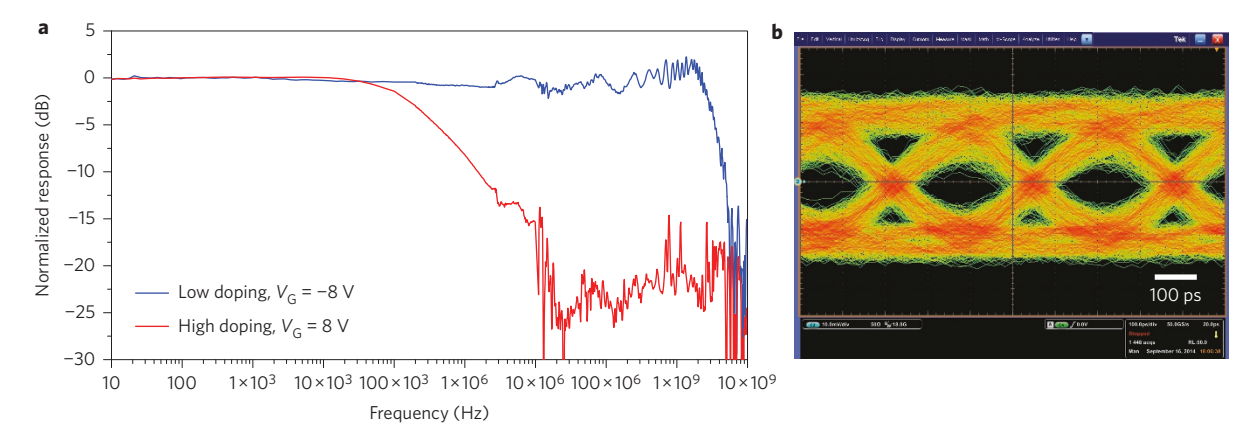


Figure 4 | Broadband frequency response of the BP photodetector. a, The response of the BP photodetector is measured when the BP is gated to low and high doping. At low doping, the response is broadband with a cutoff frequency of 3 GHz, which is limited by the RC bandwidth of the contact pads and the input impedance of the preamplifier. At high doping, the response rolls off at 0.2 MHz, indicating that the photoresponse is of a thermal origin, as expected from the bolometric effect. **b**, Receiver eye diagram at a data rate of 3 Gbit s⁻¹ measured with the BP photodetector. Scale bar, 100 ps.

the BP is gated to be highly n-doped, the photocurrent response rolls off at a much lower frequency of $f_{-3dB} = 0.2$ MHz. Because the photocurrent in this regime is due to the bolometric effect, this slower frequency response can be attributed to the low inplane lattice thermal conductivity of BP³⁴, as well as the thermal response of the silicon waveguide³⁵. The dramatically different response speed at different doping levels in the BP thus further corroborates the distinct generation mechanisms and highlights the optimized performance of the device when BP is gated to be intrinsic. To demonstrate the feasibility of using the BP device in highspeed optical communication, we also performed an eye-diagram measurement using a pseudo-random bit series (PRBS) with a data rate of 3 Gbit s⁻¹ and a low optical power of 1.2 mW (0.8 dBm). The completely open eye in Fig. 4b indicates that the BP photodetector can be readily used for practical optical communication.

In conclusion, a waveguide-integrated and gate-tunable photodetector based on few-layer BP has been demonstrated for the telecom band. High responsivity, high response speed and low dark current are achieved when the BP is gated to low doping, and the photocurrent generation is dominated by the photovoltaic effect. In nearly every aspect of their performance, BP photodetectors can outperform graphene photodetectors and are more realistic for practical use. We expect the performance of BP photodetectors to be further improved when larger flakes of BP can be exfoliated or high-quality large-scale growth of BP can be achieved. If the number of layers in BP can be controlled, its bandgap can be tailored for a specific wavelength so that both the responsivity and dark current of the photodetector are optimal. In addition, BP shows strong anisotropy in both d.c. and optical conductivity^{15,36,37}. If the armchair direction of BP can be aligned with the source-drain direction (zigzag along the waveguide) using Raman spectroscopy (Supplementary Sections 2 and 6) so that both the optical absorption and carrier mobility are maximal, the responsivity and speed of the photodetector can be maximized with a reduced device footprint. These results and the potential of BP, combined with the many previous demonstrations of optoelectronic devices based on graphene and TMDCs, indicate that two-dimensional materials and their heterostructures^{38–41} can provide the components necessary for the realization of complete optical communications links and chart a clear path towards the commercial viability of two-dimensional materials for integrated optoelectronic applications.

Methods

BP photodetectors were fabricated using SOI wafers (SOITEC) with a 110 nm top silicon layer and 3 μm buried oxide layer. The underlying photonics layer was patterned using electron-beam lithography (Vistec EBPG 5000+) with maN-2403 resist and etched with a standard silicon Bosch process to define the photonics layer. Electron-beam evaporation was then used to deposit 140 nm SiO₂ on the sample using the remaining electron-beam resist as a mask. After removing the resist in N-methylpyrrolidone (NMP) with an ultrasonic bath, the planarized substrate was annealed using rapid thermal annealing (RTA) at 1,100°C for 1 min to improve the quality of the evaporated oxide. A 10 nm layer of HfO2 was grown with ALD to protect the photonics layer from subsequent etching processes. Exfoliated BP (purchased from Smart Elements GmbH) was transferred to the planarized photonics layer with the wet transfer method described in ref. 28 (Supplementary Section 1). Care was taken to prevent the BP from making contact with the water. Photolithography and a dry etch step were used to remove unwanted material from the waveguides. Shipley S1800 series photoresist was used to protect the BP channel material during the dry etch. Source and drain contacts were defined with electronbeam lithography using poly(methyl methacrylate) (PMMA), and 5 nm Ti/50 nm Au was deposited using electron-beam evaporation at 100°C. A 20 nm ALD Al₂O₃ gate dielectric/passivation layer was then grown at 250°C. The top few-layer graphene gate was transferred using the same wet transfer method and patterned with electron-beam lithography and oxygen plasma etching. Finally, top-gate contacts were patterned using Poly(methyl methacrylate) (PMMA), and 5 nm Ti/ 30 nm Au was deposited with electron-beam evaporation.

Photocurrent maps at different biases and gate voltages were measured at a fixed wavelength for various laser powers. Two Keithley 2400 series source meters were used in this measurement, one to control the gate voltage and the other to bias the

device while measuring the source-drain current. The devices were held at a fixed gate while the bias voltage was swept twice, once with no optical power and once with the laser source on. The difference between the two scans yielded gate- and bias-dependent photocurrent. Power- and bias-dependent photocurrent were extracted from these two-dimensional scans, and the responsivity was calculated after accounting for loss from the input grating coupler, the power splitting arm of the MZI structure, and the power absorbed by the channel material.

The low-frequency photoresponse (10 Hz to 100 kHz) was measured by modulating the laser source with a high-bandwidth electro-optic modulator (EOM, Lucent 2623NA) driven by a signal generator. The photocurrent was amplified using a low-noise current preamplifier (Stanford Research Systems, SR570) and monitored with a Stanford Research Systems SR830 lock-in amplifier. The gate voltage was swept from $-10~\rm V$ to $+10~\rm V$ and the amplitude of the photocurrent was recorded at various driving frequencies. Mid-range frequencies (100 kHz to 10 MHz) were measured using a radiofrequency preamplifier and a 3 GHz bandwidth network analyser (HP 3577B). High-frequency measurements (10 MHz to 10 GHz) were achieved with a 20 GHz bandwidth network analyser (Agilent E8362B PNA). A 12 GHz photoreceiver (Newport 1554-A) was used to monitor the frequency dependence of the EOM and correct the measured frequency response. All measurements were performed at room temperature in an ambient atmosphere.

Received 23 September 2014; accepted 26 January 2015; published online 2 March 2015

References

- Xia, F., Wang, H., Xiao, D., Dubey, M. & Ramasubramaniam, A. Twodimensional material nanophotonics. *Nature Photon.* 8, 899–907 (2014).
- Avouris, P. Graphene: electronic and photonic properties and devices. Nano Lett. 10, 4285–4294 (2010).
- Bonaccorso, F., Sun, Z., Hasan, T. & Ferrari, A. C. Graphene photonics and optoelectronics. *Nature Photon.* 4, 611–622 (2010).
- Xia, F., Mueller, T., Lin, Y. M., Valdes-Garcia, A. & Avouris, P. Ultrafast graphene photodetector. *Nature Nanotech.* 4, 839–843 (2009).
- Mueller, T., Xia, F. & Avouris, P. Graphene photodetectors for high-speed optical communications. *Nature Photon.* 4, 297–301 (2010).
- Pospischil, A. et al. CMOS-compatible graphene photodetector covering all optical communication bands. Nature Photon. 7, 892–896 (2013).
- Gan, X. et al. Chip-integrated ultrafast graphene photodetector with high responsivity. Nature Photon. 7, 883–887 (2013).
- 8. Freitag, M., Low, T., Xia, F. N. & Avouris, P. Photoconductivity of biased graphene. *Nature Photon.* **7**, 53–59 (2013).
- Wang, Q. H., Kalantar-Zadeh, K., Kis, A., Coleman, J. N. & Strano, M. S. Electronics and optoelectronics of two-dimensional transition metal dichalcogenides. *Nature Nanotech.* 7, 699–712 (2012).
- 10. Mak, K. F., Lee, C., Hone, J., Shan, J. & Heinz, T. F. Atomically thin MoS₂: a new direct-gap semiconductor. *Phys. Rev. Lett.* **105**, 136805 (2010).
- Ellis, J. K., Lucero, M. J. & Scuseria, G. E. The indirect to direct band gap transition in multilayered MoS₂ as predicted by screened hybrid density functional theory. *Appl. Phys. Lett.* **99**, 261908 (2011).
- Lopez-Sanchez, O., Lembke, D., Kayci, M., Radenovic, A. & Kis, A. Ultrasensitive photodetectors based on monolayer MoS₂. Nature Nanotech. 8, 497–501 (2013).
- Li, L. et al. Black phosphorus field-effect transistors. Nature Nanotech.
 372-377 (2014).
- Liu, H. et al. Phosphorene: an unexplored 2D semiconductor with a high hole mobility. ACS Nano 8, 4033–4041 (2014).
- Xia, F., Wang, H. & Jia, Y. Rediscovering black phosphorus as an anisotropic layered material for optoelectronics and electronics. *Nature Commun.* 5, 4458 (2014).
- Das, S. et al. Tunable transport gap in phosphorene. Nano Lett. 14, 5733–5739 (2014).
- Takao, Y., Asahina, H. & Morita, A. Electronic structure of black phosphorus in tight binding approach. J. Phys. Soc. Jpn 50, 3362–3369 (1981).
- Buscema, M., Groenendijk, D. J., Steele, G. A., van der Zant, H. S. J. & Castellanos-Gomez, A. Photovoltaic effect in few-layer black phosphorus PN junctions defined by local electrostatic gating. *Nature Commun.* 5, 4651 (2014).
- Buscema, M. et al. Fast and broadband photoresponse of few-layer black phosphorus field-effect transistors. Nano Lett. 14, 3347–3352 (2014).
- Engel, M., Steiner, M. & Avouris, P. Black phosphorus photodetector for multispectral, high-resolution imaging. *Nano Lett.* 14, 6414–6417 (2014).
- Low, T., Engel, M., Steiner, M. & Avouris, P. Origin of photoresponse in black phosphorus phototransistors. *Phys. Rev. B* 90, 081408 (2014).
- Wang, H. et al. Black phosphorus radio-frequency transistors. Nano Lett. 14, 6424–6429 (2014).
- Li, H., Anugrah, Y., Koester, S. J. & Li, M. Optical absorption in graphene integrated on silicon waveguides. *Appl. Phys. Lett.* 101, 111110 (2012).
- Youngblood, N., Anugrah, Y., Ma, R., Koester, S. J. & Li, M. Multifunctional graphene optical modulator and photodetector integrated on silicon waveguides. *Nano Lett.* 14, 2741–2746 (2014).

- Gan, X. et al. Controlling the spontaneous emission rate of monolayer MoS in a photonic crystal nanocavity. Appl. Phys. Lett. 103, 181119 (2013).
- Sanfeng, W. et al. Control of two-dimensional excitonic light emission via photonic crystal. 2D Mater. 1, 011001 (2014).
- 27. Dean, C. R. et al. Boron nitride substrates for high-quality graphene electronics. *Nature Nanotech.* **5**, 722–726 (2010).
- Han, L., Neal, A. T., Mengwei, S., Yuchen, D. & Ye, P. D. The effect of dielectric capping on few-layer phosphorene transistors: tuning the Schottky barrier heights. *IEEE Electron. Dev. Lett.* 35, 795–797 (2014).
- 29. Low, T. *et al.* Tunable optical properties of multilayer black phosphorus thin films. *Phys. Rev. B* **90**, 075434 (2014).
- Hong, T. et al. Polarized photocurrent response in black phosphorus field-effect transistors. Nanoscale 6, 8978–8983 (2014).
- Xu, X. D., Gabor, N. M., Alden, J. S., van der Zande, A. M. & McEuen, P. L. Photo-thermoelectric effect at a graphene interface junction. *Nano Lett.* 10, 562–566 (2010).
- Chi On, C., Okyay, A. K. & Saraswat, K. C. Effective dark current suppression with asymmetric MSM photodetectors in Group IV semiconductors. *IEEE Photon. Technol. Lett.* 15, 1585–1587 (2003).
- Assefa, S. et al. CMOS-integrated high-speed MSM germanium waveguide photodetector. Opt. Express 18, 4986–4999 (2010).
- 34. Slack, G. A. Thermal conductivity of elements with complex lattices: B, P, S. *Phys. Rev.* **139**, A507–A515 (1965).
- 35. Pernice, W. H. P., Li, M. & Tang, H. X. Gigahertz photothermal effect in silicon waveguides. *Appl. Phys. Lett.* **93**, 213106 (2008).
- Wang, X. et al. Highly anisotropic and robust excitons in monolayer black phosphorus. Preprint at http://arXiv.org/abs/1411.1695 (2014).
- 37. Yuan, H. *et al.* Broadband linear-dichroic photodetector in a black phosphorus vertical p–n junction. Preprint at http://arXiv.org/abs/1409.4729 (2014).
- 38. Deng, Y. et al. Black phosphorus-monolayer MoS₂ van der Waals heterojunction P-N diode. ACS Nano 8, 8292–8299 (2014).

- Britnell, L. et al. Strong light–matter interactions in heterostructures of atomically thin films. Science 340, 1311–1314 (2013).
- Geim, A. K. & Grigorieva, I. V. Van der Waals heterostructures. Nature 499, 419–425 (2013).
- 41. Levendorf, M. P. *et al.* Graphene and boron nitride lateral heterostructures for atomically thin circuitry. *Nature* **488**, 627–632 (2012).

Acknowledgements

This work is supported by the Air Force Office of Scientific Research (award no. FA9550-14-1-0277) and the National Science Foundation (NSF, award no. ECCS-1351002). M.L. thanks X.H. Chen and G.J. Ye of University of Science and Technology of China for providing some of the black phosphorus samples at the initial stage of the project. Parts of this work were carried out in the University of Minnesota Nanofabrication Center, which receives partial support from the NSF through the National Nanotechnolgy Infrastructure Network (NNIN) programme, and the Characterization Facility, which is a member of the NSF-funded Materials Research Facilities Network via the Material Research Science and Engineering Center (MRSEC) programme.

Author contributions

M.L. conceived and supervised the research. N.Y. fabricated the devices, performed the measurements and analysed the data. C.C. assisted the fabrication. N.Y., M.L. and S.J.K. analysed the data. M.L., N.Y. and S.J.K. co-wrote the manuscript.

Additional information

Supplementary information is available in the online version of the paper. Reprints and permissions information is available online at www.nature.com/reprints. Correspondence and requests for materials should be addressed to M.L.

Competing financial interests

The authors declare no competing financial interests.